SCIENTIFIC REPORTS

OPEN

Spatially Resolved Thermometry of Resistive Memory Devices

Eilam Yalon[1], Sanchit Deshmukh[1], Miguel Muñoz Rojo[1], Feifei Lian[1], Christopher M. Neumann[1], Feng Xiong[1,4] & Eric Pop[1,2,3]

Received: 6 June 2017
Accepted: 11 October 2017

The operation of resistive and phase-change memory (RRAM and PCM) is controlled by highly localized self-heating effects, yet detailed studies of their temperature are rare due to challenges of nanoscale thermometry. Here we show that the combination of Raman thermometry and scanning thermal microscopy (SThM) can enable such measurements with high spatial resolution. We report temperature-dependent Raman spectra of HfO_2, TiO_2 and $Ge_2Sb_2Te_5$ (GST) films, and demonstrate direct measurements of temperature profiles in lateral PCM devices. Our measurements reveal that electrical and thermal interfaces dominate the operation of such devices, uncovering a thermal boundary resistance of 28 ± 8 m^{2}K/GW at GST-SiO_2 interfaces and an effective thermopower 350 ± 50 µV/K at GST-Pt interfaces. We also discuss possible pathways to apply Raman thermometry and SThM techniques to nanoscale and vertical resistive memory devices.

Information storage and memory devices based on the change of resistance (i.e. resistive memories or memristors) hold several key advantages over contemporary charge-based memory devices. Such memory devices are two-terminal resistors that retain their resistance state as a function of the applied voltage or current. Several technologies can be included under the general term of "resistive memory"[1,2], such as phase change memory (PCM)[3,4], resistive random access memory (RRAM)[5,6], and conductive bridge RAM (CB-RAM)[7]. Memristive devices are important not only for memory and storage applications; they are also being extensively studied as computing elements for neuromorphic architectures[2,8].

The resistive switching in RRAM devices is based on the formation and rupture of conductive filaments in thin metal oxides, like HfO_2. In PCM, a nanoscale volume of chalcogenide material (like $Ge_2Sb_2Te_5$) can be SET to a crystalline (low resistive) state and RESET to an amorphous (high resistive) state using electrical pulses. Self-heating and the local temperature play a major role in the principle of operation of both PCM[4] and RRAM[9,10]. Many of the advantages (e.g. energy efficiency improved with scaling)[11,12] and shortcomings (e.g. reliability)[13] of these technologies stem from their inherent dependence on self-heating. Therefore, understanding the energy and heat dissipation mechanism is vital for the evaluation, design and optimization of all such future technologies. However, experimental techniques to measure nanoscale device temperature are challenging and scarce[10,14,15]. In particular, spatially resolved measurements revealing energy dissipation mechanism are required for better understanding of the device physics[16,17].

Here we combine Raman thermometry and scanning thermal microscopy (SThM) to measure the spatially resolved temperature rise in resistive memory devices. This powerful combination of temperature mapping techniques has been previously used on GaN nanowires[18], but it is applied here to resistive memory devices for the first time. We present temperature-dependent Raman spectroscopy of thin films for two of the most commonly used RRAM oxides: HfO_2 and TiO_2, and for the PCM material $Ge_2Sb_2Te_5$ (GST). We then show an experimental measurement of the temperature profile in a Joule-heated PCM device, providing important insights into its operation. Finally, we discuss how Raman and SThM can be used to measure the local temperature rise in vertical and other nanoscale RRAM and PCM device geometries.

Raman Spectroscopy of RRAM Oxide Films

Raman spectroscopy measures the shift in inelastically scattered light, directly corresponding to phonon energy ($\hbar\omega$) and temperature (T). Stokes (anti-Stokes) lines are due to photons scattered at lower (higher) energy than

[1]Department of Electrical Engineering, Stanford University, Stanford, CA, 94305, USA. [2]Department of Materials Science & Engineering, Stanford University, Stanford, CA, 94305, USA. [3]Precourt Institute for Energy, Stanford University, Stanford, CA, 94305, USA. [4]Present address: Department of Electrical & Computer Engineering, University of Pittsburgh, Pittsburgh, PA, 15261, USA. Sanchit Deshmukh and Miguel Muñoz Rojo contributed equally to this work. Correspondence and requests for materials should be addressed to E.P. (email: epop@stanford.edu)

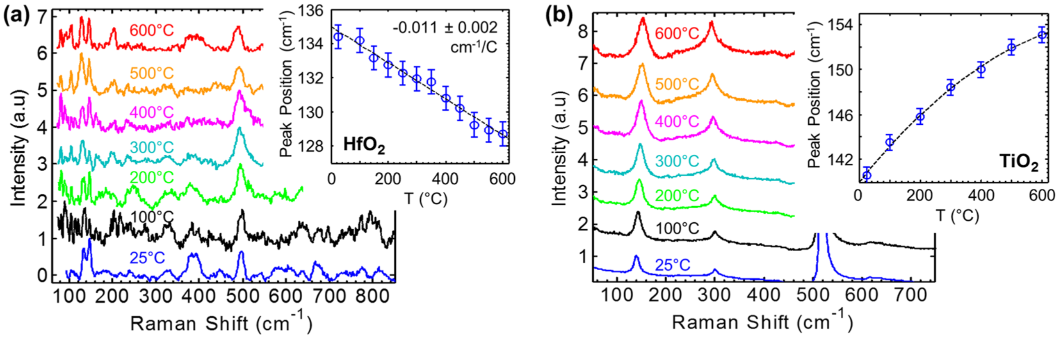

Figure 1. Temperature dependent Raman spectra of RRAM oxide nanoscale thin films. Raman spectra of crystallized 50 nm thin films of (**a**) HfO_2 and (**b**) TiO_2, measured at temperatures ranging from 25 °C to 600 °C. Spectra are vertically offset for clarity. Insets show peak position shift with temperature of a selected mode, error bars represent 95% confidence bounds of Lorentzian peak fitting. The HfO_2 was sputtered onto Pt (50 nm) on sapphire substrate and then annealed at 600 °C for 2 hours. All measured peaks above 110 cm^{-1} are assigned to monoclinic phase of HfO_2 (as confirmed by XRD)[24]. The TiO_2 was sputtered onto SiO_2 (90 nm) on Si substrate and annealed at 400 °C for 1 hour. The peak at ~141 cm^{-1} (25 °C) is assigned to anatase TiO_2 and the other peaks are from the Si substrate.

the incident laser, due to phonon emission and absorption, respectively. (More Raman spectroscopy details are given in Supplementary Information Section 1.) Fundamentally, most RRAM oxides have poor Raman signal due to weak absorption (ultra-thin films with large band gap) and low degree of crystallinity. However polycrystalline oxide film regions or the programmed RRAM filament could be expected to have different Raman signals, and are yet to be studied. For example, Raman spectroscopy has been previously used to study stoichiometry, defects, and particularly oxygen vacancies in crystalline[19] and nano-crystalline[20] oxides. The Raman spectra of oxide powders, single crystals, and thick films have previously been reported[21–23], but here we present the first temperature-dependent Raman spectra of nanoscale thin films which are relevant for RRAM devices.

Figure 1 shows the temperature-dependent Raman spectra of two of the most common RRAM oxides: (a) HfO_2 and (b) TiO_2. The 50 nm thick films were sputtered onto Pt/sapphire and SiO_2/Si substrates, respectively, and did not show any measurable Raman features in their (as-deposited) amorphous state. After annealing (see Methods) the films crystallized, exhibiting Raman signals of the monoclinic (HfO_2) and anatase (TiO_2) phases. The insets show the temperature dependence of a selected mode. The B_{g1} monoclinic HfO_2 mode[24] (~134 cm^{-1} at 25 °C) shows typical frequency downshift with temperature at rate of ~ -0.011 cm^{-1}/C. The E_g anatase TiO_2 mode (~141 cm^{-1} at 25 °C) however shows anomalous frequency increase with temperature. This trend was previously reported and explained via strong contribution of the quartic anaharmonicity[23]. For the practical purpose of device thermometry it is sufficient to have a well-defined temperature response of the Raman mode, either positive or negative.

We note that temperature-dependent Raman data are presented in this section for nanoscale oxide films for the first time. However, obtaining sufficient signal in nanoscale RRAM *devices* is challenging, but could be addressed using signal enhancement techniques such as surface- or tip- enhanced Raman spectroscopy (SERS[25] or TERS[26,27]). In addition, an optically transparent electrode such as graphene[28], indium tin oxide (ITO), or a very thin (e.g. sub-10 nm) metal can be used to measure vertical device structures. In the next section we focus on Raman thermometry of PCM, which exhibits a sufficiently strong signal to demonstrate (spatial) device thermometry.

RAMAN Spectroscopy of PCM

Raman Spectroscopy of GST Films. Raman spectroscopy has previously been used to characterize nanoscale PCM films[29–31]. Unlike oxides, GST absorbs photons in the range of visible excitation lasers (~500–650 nm) due to its smaller band gap (~0.6 eV). In addition, much of the GST volume in a typical PCM cell is crystalline, thus Raman thermometry can be readily applied to PCM devices. Moreover, Raman spectroscopy can be used to identify phase and presence of defects in GST as outlined below.

Figure 2 shows the temperature dependent Raman signal of 20 nm thin sputtered GST films (see Methods). Some previous studies have performed such measurements on 50 to 150 nm thick GST films[32–34] but we are unaware of temperature-dependent Raman data for GST films of the thickness studied here (~20 nm), which are more relevant for modern memory devices. Figure 2(a) shows the first heating cycle on a hot stage from 25 °C to 400 °C. The as-deposited film is amorphous (a-GST) and starts to crystallize (c-GST) at ~140 °C, first to the face centered cubic (fcc) phase and then at ~240 °C to the hexagonal closest pack (hcp) phase. For assignment of the various Raman peaks to GST modes please see ref.[29]. Upon cooling to room temperature and heating back up to 450 °C the film remains in its stable hcp phase, as shown in Fig. 2(b). Figure 2(c) shows the measured (symbols) and fitted peak of a selected mode at stage temperatures of 25 °C (blue, ~173 cm^{-1}) and 400 °C (red, ~168 cm^{-1}) and Fig. 2(d) shows the peak position downshifting vs. stage temperature from 25 °C to 450 °C.

Raman Spectroscopy of GST Devices. Thanks to its material and phase selectivity, Raman spectroscopy can be used to map GST films and PCM devices for phase analysis. However, here we uncover that patterned and

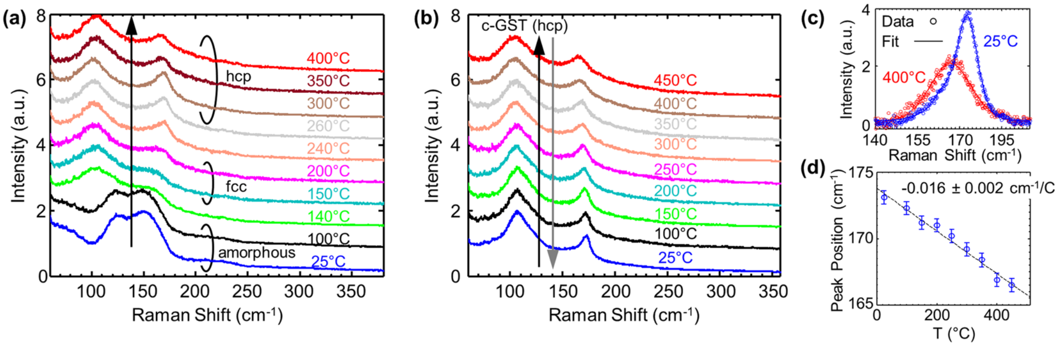

Figure 2. Temperature dependent Raman spectra of 20 nm thin GST film. (See Methods). (**a**) Raman spectra during the first heating cycle on a hot stage from 25 °C to 400 °C. As-deposited, the GST is amorphous, but after heating the film starts to crystallize first to the fcc phase and then to the hcp phase. (**b**) Temperature dependent Raman spectra of the stable hcp phase GST at temperatures ranging from 25 °C to 450 °C. Similar spectra were obtained for cooling (not shown). (**c**) Example of measured (symbols) and fitted (lines) peak for a selected mode at 25 °C and 400 °C in the hcp phase. (**d**) Peak position shift vs. temperature of the selected mode shown in (**c**). Error bars represent 95% confidence bounds of Lorentzian peak fitting.

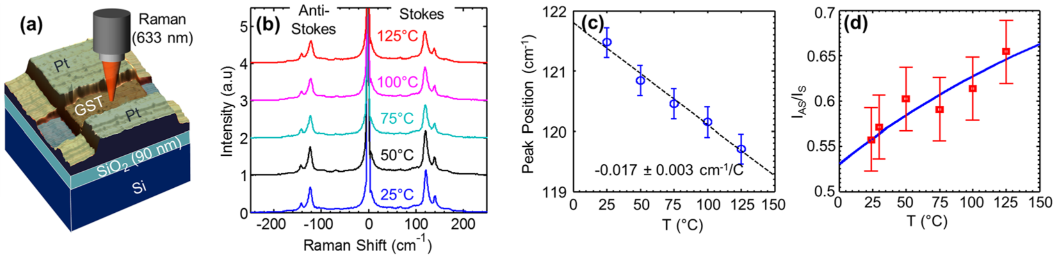

Figure 3. Temperature dependent Raman spectra of lateral GST device. (**a**) Device and measurement setup. The GST channel ($W = 10\,\mu m$, $L = 5\,\mu m$) is patterned on top of Pt electrodes and capped with PMMA (see Methods). (**b**) Stokes and anti-Stokes Raman spectra of patterned GST device on a hot stage at temperatures from 25 °C to 125 °C. These are dominated by Te modes[35] with much higher intensity than GST modes. (**c**) Peak shift with temperature of a selected mode (at ~120 cm^{-1}). (**d**) Anti-Stokes to Stokes intensity ratio vs. temperature of the selected mode shown in (c).

processed GST *devices* exhibit Raman spectra that are different from blanket deposited GST *films*. Figure 3(a) schematically shows the Raman measurement of a lateral GST device with Pt contacts, and device fabrication details are provided in the Methods section.

Figure 3(b) shows the Stokes and anti-Stokes Raman signal of the GST device on a hot stage from 25 °C to 125 °C. The stage temperature was kept below the highest temperature during processing (PMMA bake at 180 °C) in order to avoid changes to the GST channel and/or contacts. It is evident that the Raman signal of the GST device is dominated by two intense peaks at ~120 and ~140 cm^{-1}, which are not present in the GST film spectra (Fig. 2). These peaks were present in the GST device immediately after lift-off, before spin-coating the PMMA capping. The intensity of these peaks is significantly larger than the GST film peaks shown in Fig. 2.

These intense peaks (~120 and ~140 cm^{-1}) are known from previous studies as Te peaks[35]. We have also measured similar peaks in uncapped GST films after exposure to high laser power and formation of dark spots in the film (Supplementary Information Section 2). These peaks were also measured in other sets of lateral GST devices which were capped with different oxides[36]. Such oxide-capped devices switched for many cycles (~10^5) with good on/off ratio (~10^2) and low switching energy (<20 pJ). These Te peaks are likely associated with surface oxidation of the GST during processing, resulting in formation of GeO_x and SbO_x, and precipitation of Te. The former is also evident from X-Ray photoelectron spectroscopy (XPS) of the dark spots at the GST surface (Supplementary Information Section 2), while the latter is evidenced in our measured Raman spectra.

The position of the lower (~120 cm^{-1}) Te peak has strong temperature dependence, as shown in Fig. 3(c) which allows us to use it efficiently as a thermometer. Raman spectroscopy can then be used to extract temperature in two different ways; one via the calibration of peak shift vs. temperature on the hot stage[37,38] and the other directly from the anti-Stokes to Stokes (AS/S) intensity ratio[39]:

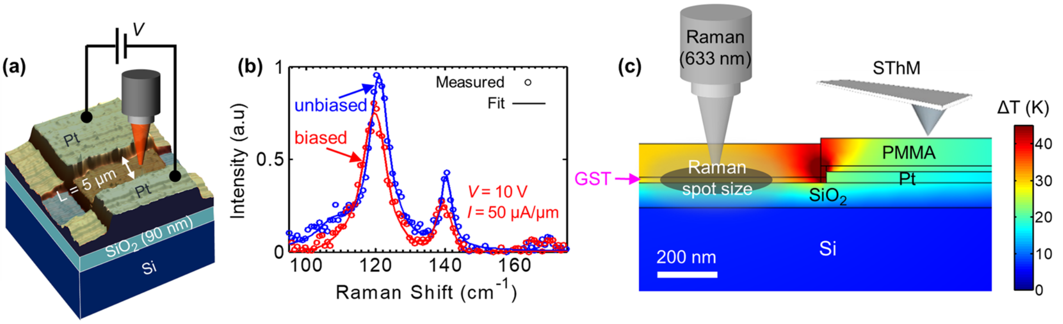

Figure 4. Thermometry of a lateral PCM device. (**a**) Measurement setup: Raman (and SThM) acquired during device operation with self-heating. (**b**) Measured (symbols) and fitted (lines) Raman spectra of the GST at the center of the channel with electrical bias (red: $V = 10\,\text{V}$, $I = 0.5\,\text{mA}$) and without bias (blue). (**c**) Simulated cross-section temperature profile of the device near the contact, highlighting the temperature measured by Raman (directly on GST film with Gaussian laser spot size) and SThM (top surface of PMMA capping layer).

$$T = \frac{\hbar\omega_{\text{ph}}}{k_{\text{B}}}\left[3\,\ln\left(\frac{\omega_{\text{L}} + \omega_{\text{ph}}}{\omega_{\text{L}} - \omega_{\text{ph}}}\right) - \ln(I_{\text{AS}}/I_{\text{S}})\right]^{-1} \tag{1}$$

where T is the phonon temperature (in K), ω_{ph} and ω_{L} are the phonon shift and laser frequency, respectively, $I_{\text{AS}}/I_{\text{S}}$ the anti-Stokes to Stokes intensity ratio, and k_{B} is the Boltzmann constant. The advantage of the AS/S method is that in principle it does not require a calibration procedure and that the temperature can be obtained with a single measurement. This is attractive for spatial temperature mapping of devices since the temperature map can be obtained in a single map scan, whereas for the peak shift method a calibration measurement is needed and at least two map scans must be obtained[38] (e.g. one with and the other without bias). Nonetheless, the uncertainty in the measured temperature of our GST devices using the AS/S method was large compared with the peak shift method, as described below.

The symbols in Fig. 3(d) show the measured AS/S intensity ratio of the spectra from Fig. 3(b) after baseline subtraction and Lorentzian peak fitting. The error bars are obtained from the standard deviation of ~30 measurements (carried out at ambient $T = 25\,°\text{C}$). The blue line represents eq. (1). The main drawback of the AS/S method is the uncertainty in the temperature evaluation, because the extraction of intensity from peak fitting is less accurate than the extraction of peak position. (Similar errors are encountered when using the *area* under the peak instead of the peak intensity.) Moreover, the *absolute* temperature T ($\geq 300\,\text{K}$) is obtained from the intensity ratio with relative error ~15% in our case. Since we are interested in measuring the *change* in temperature ($\Delta T \sim 100\,\text{K}$ above room temperature) the relative error in ΔT is three times larger, or nearly ~ 50%. At the same time, the relative error in ΔT for the peak shift method is less than ~15% [e.g. see Fig. 3(c)]. Therefore, in the remainder of this study we use the peak shift method to map the temperature of the device, following the procedure outlined in ref.[38] for aligning the two maps. We note that temperature sensitivity of the AS/S method should improve for phonon modes at higher frequencies (Supplementary Information Section 3).

PCM Device Thermometry

Measurement Technique. Figure 4(a) displays the schematic of the Raman thermometry measurement applied to a lateral GST device. We spatially mapped the device with 0.25 µm step size, measuring the Raman spectra at each point with and without electrical bias. The temperature is extracted by converting the peak shift (with electrical bias and self-heating) to temperature via the calibration shown in Fig. 3(c). Figure 4(b) shows the measured (symbols) and fitted (lines) Raman spectra at the center of the GST channel with (red) and without (blue) electrical bias. The Te peaks at ~120 and 140 cm^{-1} are clearly visible, as well as their shift with self-heating. Raman features at ~105 and 170 cm^{-1} may correspond to GST hcp phase, but their signal is significantly smaller.

We also carried out scanning thermal microscopy (SThM) measurements on the same devices. SThM is an atomic force microscopy (AFM) based technique that uses a thermo-resistive probe to acquire nanoscale topographic and thermal images simultaneously[40,41]. Unlike Raman, SThM measures only the surface temperature and requires additional calibration (see Supplementary Information Section 4), however it provides nearly AFM-like spatial resolution (<100 nm) and is therefore used here to provide complementary insight into PCM device thermometry.

Figure 4(c) shows the simulated cross-sectional temperature profile in our lateral GST device and contact. Three-dimensional (3D) finite element simulations were carried out using COMSOL Multiphysics®. To better understand the measurements, we illustrate the Raman and SThM instruments with the cross-sectional simulated temperature. The Raman method measures the temperature of the GST channel but its signal is averaged across the Gaussian laser beam spot (here ~ 400 nm). Inherently the SThM has better spatial resolution with a thermal exchange radius of <100 nm[42], yet it measures the temperature at the top surface of the PMMA capping layer which spreads the heat. Simulations therefore predict slightly different temperature profiles for the Raman

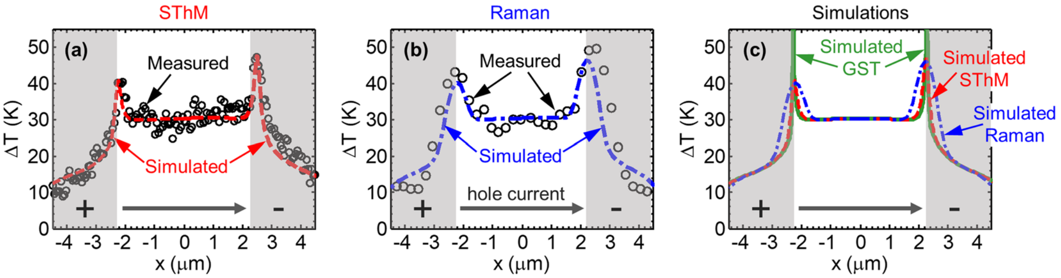

Figure 5. Measured vs. simulated temperature rise. Temperature rise along GST channel in fcc phase (black symbols) measured by (**a**) SThM and (**b**) Raman thermometry. The gray zones mark the contact regions. The simulated temperature rise fitted by finite element modeling for SThM (red dashed line) and Raman (blue dash-dot line) are also shown in (**a**) and (**b**) respectively. (**c**) Simulated temperature rise of the GST channel (green solid line), the SThM (top of PMMA surface averaged across thermal exchange radius[42]) same as in (**a**) and Raman (GST with Gaussian laser spot size) same as in (**b**). Black arrows mark hole current flow direction.

and SThM measurements. We note that the SThM is operated here in DC mode and is not calibrated to output temperature directly, rather it outputs a relative signal. We then use Raman thermometry (with same power input conditions) to calibrate the SThM to the temperature in the middle of the PCM device, where the GST temperature (measured by Raman) and the top PMMA temperature (measured by SThM) are similar [see cross-sectional temperature rise in Fig. 4(c)]. This calibration is made possible by the fact that the device temperature is uniform across several microns in the center of the GST channel, a region larger than the laser spot size.

The main advantage of the Raman measurement is its material selectivity which allows a differential measurement of materials in the laser path, thus enabling even atomic scale resolution in the cross-plane direction[43]. However, not all materials have a usable Raman signal and the spatial resolution is diffraction-limited (unless a signal enhancement technique such as TERS[26] is utilized). SThM on the other hand has nearly AFM-like spatial resolution, but measures the temperature at the top surface rather than the direct temperature of the material of interest. The temperature sensitivity of the SThM can be better than that of the Raman method, but in order to convert the SThM signal (voltage) to temperature, the Raman method was used for calibration, as outlined above. Both techniques are limited in measuring *vertical* RRAM devices; the top electrode might block the Raman signal and laterally spread the temperature profile measured by SThM. Nonetheless, the combination of both techniques could become a very powerful tool to study the power dissipation in cases where temperature plays a major role in device operation[2,3,5,10]. A practical solution is to measure lateral devices or vertical devices having transparently thin top electrode.

Power Dissipation in Lateral PCM Device. Figure 5 compares the temperature profile along the device channel (including the contacts) measured by (a) SThM and (b) Raman to the simulated temperature rise with very good agreement. The full device temperature maps are shown in Supplementary Information Sections 5 and 6. Figure 5(c) shows the simulated temperature rise of the GST channel (green) as well as the profile that would be measured by SThM (red) and Raman (blue). Figure 5 highlights how the power dissipation in our devices is revealed via both Raman thermometry and SThM, with varying degrees of spatial accuracy. By inspecting the measured temperature profiles in Fig. 5 and the fitting parameters used in the simulation (summarized in Table I of Supplementary Information Section 9), several conclusion can be drawn as follows.

First, it is evident that significant heat is generated at the contacts[44]. Temperature artifacts due to the presence of step heights at the edge of the GST-Pt contacts are negligible here compared with the observed interfacial heating as discussed in Supplementary Information Section 6. It appears that the large contact resistivity of the GST film on the Pt contact (GST is deposited on top of the Pt electrodes) leads to highly localized power density, mainly at the edge of the electrode (also evident in the SThM maps shown in Supplementary Information Section 5). We also carried out transfer length method (TLM) measurements to directly extract the contact and sheet resistance (Supplementary Information Section 7) which served as inputs to the simulations. However, the temperature peak at the Pt-GST edge suggests that much of the contact voltage may be dropped at the imperfect GST step coverage of the Pt electrodes. To account for this, we set the GST resistivity at the Pt sidewall to be 20x larger than the bulk GST resistivity, leading to correct fitting in our simulations. The temperature rise of the 5 μm long GST channel suggests that much of the power dissipates there, yet the temperature peaks at the contacts due to the high power *density* there.

Second, given the power input and the measured temperature rise we can extract the thermal boundary resistance (TBR) of the GST-SiO_2 and GST-Pt interfaces to be 28 ± 8 and 25 ± 9 m^2K/GW respectively. Since the Si and SiO_2 thermal properties are well known, and given the insensitivity to the bulk GST thermal conductivity (see Supplementary Section 9) the GST-SiO_2 TBR acts as a single fitting parameter to the temperature rise at the center of the PCM device. The obtained value is in agreement with the TBR of the GST-SiO_2 interface previously measured[45] by the time domain thermo-reflectance (TDTR) technique, but it is extracted here within a functioning PCM device for the first time. The measured TBR of the GST-SiO_2 interface is equivalent to a Kapitza length of ~50 nm of SiO_2, which accounts for more than 25% of the total thermal resistance in our device. Importantly, the relative contribution of the TBR is expected to increase and dominate as devices are scaled down in size[46].

Third, we also observe a clear asymmetry in heating at the two contacts, with the higher temperature at the edge of the grounded electrode. This contact heating asymmetry is due to a combination of thermoelectric and thermionic effects[17,47] as confirmed by reversing the current flow direction. We extract an effective thermopower $S = 350 \pm 50$ μV/K, which includes both thermoelectric and thermionic effects at the GST-Pt contact. Similar values were reported for GST in the mixed amorphous and fcc phase with Pt[48] and with TiW[49] contacts slightly above room temperature, after annealing up to ~ 150 °C. Following anneal at higher temperature (>200 °C) and higher degree of crystallization, the thermopower is expected to drop significantly (below 50 μV/K)[48,49]. The higher temperature at the grounded contact is also consistent with the location of damage after device breakdown, shown in Supplementary Information Section 8. The asymmetric heating highlights the importance of designing the voltage polarity of PCM programming pulses, to take advantage of thermionic and thermoelectric effects[50]. We note that our test devices are lateral and larger than state-of-the-art PCM devices[51–54]; however the physical insights are valid and highly valuable: the power generation is dominated by electrical contacts and the heat dissipation is limited by thermal interfaces in nanoscale devices[44].

Conclusion

In summary, in this study we have laid the fundamental basis for thermometry of RRAM and PCM data storage devices. We presented the first measurements of thermal Raman signatures in nanoscale films of HfO_2 and TiO_2, and we used spatial mapping of temperature (with both Raman and SThM) to provide physical insight into the operation of PCM devices. Our approach takes advantage of the benefits of each technique, e.g. selectivity (Raman) and high spatial resolution (SThM), and can be extended to a wide variety of devices. We uncover significant heating at the contacts, suggesting that power dissipation is often dominated by electrical contact resistance. Contact heating is asymmetric, depending on current flow direction, showing that thermoelectric effects must be taken into account when designing PCM programming pulses. We also extract the TBR of the GST-SiO_2 interface and find that it is equivalent to ~ 50 nm thick SiO_2, contributing much of the device thermal resistance. The role of both electrical contacts and thermal interfaces will only become more dominant as devices are scaled to sub-50 nm dimensions. Uncovering the spatial distribution of temperature rise in such self-heated memristive devices is essential for their understanding, and their future design and integration.

Methods

Raman measurements were carried out on a Horiba Labram Evolution HR using a 633 nm laser with an 1800 l/mm grating. The red laser is chosen here since it provides Raman signal comparable to other laser lines in our system (e.g. 532 nm) and allows the measurement of anti-Stokes signal by using a volume Bragg grating optical filter at 633 nm. All measurements were done in air.

HfO_2 films were deposited by reactive sputtering from an Hf target in an Ar:O_2 (7:3) plasma at 4 mTorr, with a forward RF power of 150 W, at room temperature onto thin Pt films (50 nm) on a sapphire substrate. The Pt/sapphire substrate was used to enhance the Raman signal of the HfO_2 film. TiO_2 films were sputtered from a Ti target in an Ar:O_2 (14:1) plasma at 5 mTorr onto SiO_2 (90 nm) on Si substrates. To obtain Raman signal the films were crystallized by annealing: the TiO_2 for 1 hour at 400 °C and the HfO_2 for 2 hours at 600 °C, both in air.

Blanket GST films (20 nm) discussed in the section "Raman Spectroscopy of GST Films" were sputtered onto SiO_2 (90 nm) on Si substrates, immediately followed (without breaking chamber vacuum) by sputtering 20 nm SiO_2 to prevent oxidation when later exposed to air. GST devices (section "Raman Spectroscopy of GST Devices") were prepared as follows. First, contacts and pads were defined by photolithography. Contact separation defined channel lengths $L = 2$ to 20 μm. The 40 nm Pt contacts (with 2 nm Ti adhesion layer) were then deposited by e-beam evaporation followed by patterning of channels (of widths $W = 1$ to 10 μm) with e-beam lithography, sputtering of 20 nm GST and lift-off. Devices were capped by spin coating ~150 nm poly(methyl methacrylate) (PMMA) to prevent oxidation, then baked on a hot plate at 180 °C for 10 minutes (in air) to crystallize the GST film.

The SThM measurements were carried out in passive mode and under DC bias. Measured PCM devices were Joule heated electrically by applying constant voltage to the contact pads for ~10 minutes during the SThM scan. The SThM thermal probe model used in this work is a DM-GLA-5 from Anasys®, which is made of a thin Pd layer on SiN.

References

1. Strukov, D. B., Snider, G. S., Stewart, D. R. & Williams, R. S. The missing memristor found. *Nature* **453**, 80–83 (2008).
2. Yang, J. J., Strukov, D. B. & Stewart, D. R. Memristive devices for computing. *Nature Nanotechnology* **8**, 13–24 (2012).
3. Wong, H.-S. P. *et al.* Phase change memory. *Proceedings of the IEEE* **98**, 2201–2227 (2010).
4. Raoux, S., Xiong, F., Wuttig, M. & Pop, E. Phase change materials and phase change memory. *MRS bulletin* **39**, 703–710 (2014).
5. Wong, H.-S. P. *et al.* Metal–oxide RRAM. *Proceedings of the IEEE* **100**, 1951–1970 (2012).
6. Waser, R., Dittmann, R., Staikov, G. & Szot, K. Redox-Based Resistive Switching Memories–Nanoionic Mechanisms, Prospects, and Challenges. *Advanced Materials* **21**, 2632–2663 (2009).
7. Valov, I., Waser, R., Jameson, J. R. & Kozicki, M. N. Electrochemical metallization memories—fundamentals, applications, prospects. *Nanotechnology* **22**, 254003 (2011).
8. Prezioso, M. *et al.* Training and operation of an integrated neuromorphic network based on metal-oxide memristors. *Nature* **521**, 61–64 (2015).
9. Larentis, S., Nardi, F., Balatti, S., Gilmer, D. C. & Ielmini, D. Resistive switching by voltage-driven ion migration in bipolar RRAM—Part II: Modeling. *IEEE Transactions on Electron Devices* **59**, 2468–2475 (2012).
10. Yalon, E. *et al.* Thermometry of Filamentary RRAM Devices. *IEEE Transactions on Electron Devices* **62**, 2972–2977 (2015).
11. Xiong, F., Liao, A. D., Estrada, D. & Pop, E. Low-power switching of phase-change materials with carbon nanotube electrodes. *Science* **332**, 568–570 (2011).
12. Xiong, F. *et al.* Self-aligned nanotube–nanowire phase change memory. *Nano Letters* **13**, 464–469 (2013).
13. Ielmini, D., Sharma, D., Lavizzari, S. & Lacaita, A. L. Reliability impact of chalcogenide-structure relaxation in phase-change memory (PCM) cells—Part I: Experimental study. *IEEE Transactions on Electron Devices* **56**, 1070–1077 (2009).
14. Yalon, E., Cohen, S., Gavrilov, A. & Ritter, D. Evaluation of the local temperature of conductive filaments in resistive switching materials. *Nanotechnology* **23**, 465201 (2012).

15. Sharma, A. A., Noman, M., Skowronski, M. & Bain, J. A. High-speed in-situ pulsed thermometry in oxide RRAMs. In *2014 International Symposium on VLSI Technology, Systems and Application* (*VLSI-TSA*). (IEEE, https://doi.org/10.1109/VLSI-TSA.2014.6839687).
16. Grosse, K. L., Bae, M.-H., Lian, F., Pop, E. & King, W. P. Nanoscale Joule heating, Peltier cooling and current crowding at graphene-metal contacts. *Nature Nanotechnology* **6**, 287–290 (2011).
17. Grosse, K. L., Xiong, F., Hong, S., King, W. P. & Pop, E. Direct observation of nanometer-scale Joule and Peltier effects in phase change memory devices. *Applied Physics Letters* **102**, 193503 (2013).
18. Soudi, A., Dawson, R. D. & Gu, Y. Quantitative heat dissipation characteristics in current-carrying GaN nanowires probed by combining scanning thermal microscopy and spatially resolved Raman spectroscopy. *ACS Nano* **5**, 255–262 (2011).
19. Tenne, D. *et al*. Raman study of oxygen reduced and re-oxidized strontium titanate. *Physical Review B* **76**, 024303 (2007).
20. Kosacki, I., Suzuki, T., Anderson, H. U. & Colomban, P. Raman scattering and lattice defects in nanocrystalline CeO_2 thin films. *Solid State Ionics* **149**, 99–105 (2002).
21. Li, C. W., McKerns, M. M. & Fultz, B. Raman spectrometry study of phonon anharmonicity of hafnia at elevated temperatures. *Physical Review B* **80**, 054304 (2009).
22. Quintard, P. E., Barbéris, P., Mirgorodsky, A. P. & Merle-Méjean, T. Comparative Lattice-Dynamical Study of the Raman Spectra of Monoclinic and Tetragonal Phases of Zirconia and Hafnia. *Journal of the American Ceramic Society* **85**, 1745–1749 (2002).
23. Ohsaka, T. Temperature dependence of the Raman spectrum in anatase TiO_2. *Journal of the Physical Society of Japan* **48**, 1661–1668 (1980).
24. Gao, L. *et al*. Effect of oxygen vacancies and strain on the phonon spectrum of HfO_2 thin films. *Journal of Applied Physics* **121**, 224101 (2017).
25. Stiles, P. L., Dieringer, J. A., Shah, N. C. & Van Duyne, R. P. Surface-enhanced Raman spectroscopy. *Annu. Rev. Anal. Chem.* **1**, 601–626 (2008).
26. Deckert, V. Tip-Enhanced Raman Spectroscopy. *Journal of Raman Spectroscopy* **40**, 1336–1337 (2009).
27. Stöckle, R. M., Suh, Y. D., Deckert, V. & Zenobi, R. Nanoscale chemical analysis by tip-enhanced Raman spectroscopy. *Chemical Physics Letters* **318**, 131–136 (2000).
28. Baeumer, C. *et al*. Spectromicroscopic insights for rational design of redox-based memristive devices. *Nature Communications* **6**, 8610 (2015).
29. Němec, P. *et al*. Amorphous and crystallized Ge–Sb–Te thin films deposited by pulsed laser: Local structure using Raman scattering spectroscopy. *Materials Chemistry and Physics* **136**, 935–941 (2012).
30. Kolobov, A. V. *et al*. Understanding the phase-change mechanism of rewritable optical media. *Nature Materials* **3**, 703–708 (2004).
31. Andrikopoulos, K., Yannopoulos, S., Kolobov, A., Fons, P. & Tominaga, J. Raman scattering study of GeTe and $Ge_2Sb_2Te_5$ phase-change materials. *Journal of Physics and Chemistry of Solids* **68**, 1074–1078 (2007).
32. Tominaga, J. & Atoda, N. Study of the crystallization of GeSbTe films by Raman spectroscopy. *Japanese Journal of Applied Physics* **38**, L322 (1999).
33. Wu, Y., Liu, K., Li, D., Guo, Y. & Pan, S. *In situ* AFM and Raman spectroscopy study of the crystallization behavior of $Ge_2Sb_2Te_5$ films at different temperature. *Applied Surface Science* **258**, 1619–1623 (2011).
34. Guo, S. *et al*. Temperature and concentration dependent crystallization behavior of $Ge_2Sb_2Te_5$ phase change films: tungsten doping effects. *RSC Advances* **4**, 57218–57222 (2014).
35. Pine, A. & Dresselhaus, G. Raman spectra and lattice dynamics of tellurium. *Physical Review B* **4**, 356 (1971).
36. Fong, S. J. *et al*. Dual-layer Dielectric Stack for Thermally-isolated Low-energy Phase-change Memory. *IEEE Transactions on Electron Devices* **64**, 4496–4502 (2017).
37. Freitag, M. *et al*. Energy dissipation in graphene field-effect transistors. *Nano Letters* **9**, 1883–1888 (2009).
38. Yalon, E. *et al*. Energy Dissipation in Monolayer MoS_2 Electronics. *Nano Letters* **17**, 3429–3433 (2017).
39. Kip, B. J. & Meier, R. J. Determination of the local temperature at a sample during Raman experiments using Stokes and anti-Stokes Raman bands. *Applied Spectroscopy* **44**, 707–711 (1990).
40. Majumdar, A. Scanning thermal microscopy. *Annual Review of Materials Science* **29**, 505–585 (1999).
41. Borca-Tasciuc, T. Scanning probe methods for thermal and thermoelectric property measurements. *Annu. Rev. Heat Transfer* **16**, 211–258 (2013).
42. Puyoo, E., Grauby, S., Rampnoux, J.-M., Rouvière, E. & Dilhaire, S. Thermal exchange radius measurement: Application to nanowire thermal imaging. *Review of Scientific Instruments* **81**, 073701 (2010).
43. Chen, C.-C., Li, Z., Shi, L. & Cronin, S. B. Thermal interface conductance across a graphene/hexagonal boron nitride heterojunction. *Applied Physics Letters* **104**, 081908 (2014).
44. Xiong, F., Yalon, E., Behnam, A., Neumann, C., Grosse, K., Deshmukh, S. & Pop, E. Towards ultimate scaling limits of phase-change memory. In 2016 *IEEE International Electron Devices Meeting* (*IEDM*). 4.1.1–4.1.4 (IEEE, https://doi.org/10.1109/IEDM.2016.7838342).
45. Battaglia, J.-L. *et al*. Thermal characterization of the SiO_2-$Ge_2Sb_2Te_5$ interface from room temperature up to 400 °C. *Journal of Applied Physics* **107**, 044314 (2010).
46. Reifenberg, J. P., Kencke, D. L. & Goodson, K. E. The impact of thermal boundary resistance in phase-change memory devices. *IEEE Electron Device Letters* **29**, 1112–1114 (2008).
47. Pop, E. Energy dissipation and transport in nanoscale devices. *Nano Research* **3**, 147–169 (2010).
48. Lee, J., Kodama, T., Won, Y., Asheghi, M. & Goodson, K. E. Phase purity and the thermoelectric properties of $Ge_2Sb_2Te_5$ films down to 25 nm thickness. *Journal of Applied Physics* **112**, 014902 (2012).
49. Grosse, K. L., Pop, E. & King, W. P. Heterogeneous nanometer-scale Joule and Peltier effects in sub-25 nm thin phase change memory devices. *Journal of Applied Physics* **116**, 124508 (2014).
50. Lee, J., Asheghi, M. & Goodson, K. E. Impact of thermoelectric phenomena on phase-change memory performance metrics and scaling. *Nanotechnology* **23**, 205201 (2012).
51. Kim, I. *et al*. High performance PRAM cell scalable to sub-20nm technology with below $4F^2$ cell size, extendable to DRAM applications. In *2010 Symposium on VLSI Technology* (*VLSIT*). 203–204 (IEEE, https://doi.org/10.1109/VLSIT.2010.5556228).
52. Kau, D. *et al*. A stackable cross point Phase Change Memory. In *2009 IEEE International Electron Devices Meeting* (*IEDM*). 617–620 (IEEE, https://doi.org/10.1109/IEDM.2009.5424263).
53. Kinoshita, M. *et al*. Scalable 3-D vertical chain-cell-type phase-change memory with $4F^2$ poly-Si diodes. In *2012 Symposium on VLSI Technology* (*VLSIT*). 35–36 (IEEE, https://doi.org/10.1109/VLSIT.2012.6242448).
54. Ahn, S. *et al*. Highly manufacturable high density phase change memory of 64Mb and beyond. In *2004 IEEE International Electron Devices Meeting* (*IEDM*). 907–910 (IEEE, https://doi.org/10.1109/IEDM.2004.1419329).

Acknowledgements

We thank Ajay Sood, Scott Fong and Ilya Karpov for helpful discussions. We acknowledge the Stanford Nanofabrication Facility (SNF) and Stanford Nano Shared Facilities (SNSF) for enabling device fabrication and measurements. This work was supported in part by the NSF Center for Power Optimization of Electro-Thermal Systems (POETS), by the NSF grant DMREF 1534279, by DARPA Matrix program (HRL Laboratories subcontract), and by the Stanford Non-Volatile Memory Technology Research Initiative (NMTRI). E.Y. acknowledges partial support from Ilan Ramon Fulbright Fellowship and from Andrew and Erna Finci Viterbi Foundation.

Author Contributions

E.Y. and E.P. conceived the idea and designed the experiments. S.D. deposited the films and fabricated the devices. E.Y. performed the Raman measurements and analysis. M.M.R. carried out the AFM measurements. M.M.R. and E.Y. carried out the SThM measurements. E.Y. performed the electro-thermal modeling. F.L. assisted with Raman measurements. C.M.N. and F.X. assisted with Raman analysis. E.Y. and E.P. wrote the manuscript. All authors discussed the results and commented on the manuscript.

Additional Information

Supplementary information accompanies this paper at https://doi.org/10.1038/s41598-017-14498-3.

Competing Interests: The authors declare that they have no competing interests.

Spatially Resolved Thermometry of Resistive Memory Devices

Eilam Yalon[1], Sanchit Deshmukh[1,†], Miguel Muñoz Rojo[1,†], Feifei Lian[1], Christopher M. Neumann[1], Feng Xiong[1,2], and Eric Pop[1,3,4,*]

[1]*Department of Electrical Engineering, Stanford University, Stanford, CA 94305, USA.* [2]*Present address: Department of Electrical & Computer Engineering, University of Pittsburgh, Pittsburgh, PA 15261, USA.* [3]*Department of Materials Science & Engineering, Stanford University, Stanford, CA 94305, USA.* [4]*Precourt Institute for Energy, Stanford University, Stanford, CA 94305, USA.* [*]*E-mail: epop@stanford.edu*

[†]*Authors contributed equally*

Supplementary Information

Table of Contents

1. Raman spectroscopy

Raman spectroscopy measures the shift in inelastically scattered light, directly corresponding to phonon energy ($\hbar\omega$) and temperature (T). Stokes (anti-Stokes) lines are due to photons scattered at lower (higher) energy than the incident laser, due to phonon emission and absorption, respectively. Thus, the Raman scattering process directly probes the phonon modes in the sample and provides information on the atomic structure, while also being sensitive to strain[1], doping[2], defects[3], and temperature[4,5]. The sensitivity to temperature arises from phonon mode softening (peak position downshift) as well as increased phonon scattering (peak broadening) with increasing temperature. In addition, the anti-Stokes to Stokes intensity ratio depends on the phonon population which is directly related to temperature[6]. The capability of measuring nanoscale features (such as individual carbon nanotubes)[7] combined with the sensitivity to temperature result in a potentially attractive technique for RRAM and PCM thermometry. Other details of the Raman measurements carried out in this work are presented in the Methods section of the paper.

2. Raman signal of patterned GST devices

We studied the origin of the Raman features found in our patterned GST devices which show a different spectra compared with blanket deposited GST (see Figs. 2 and 3 in the main text). The Raman spectra of our patterned GST devices is shown in Fig. S1(a) (red) and includes two prominent features: one at ~122 cm^{-1} and the other at ~142 cm^{-1} which are clearly associated with the presence of Te [Fig. S1(e-g)][8]. We compare the patterned GST Raman spectra with that of other GST films that most likely oxidized during laser-induced heating [Fig. S1(b)] and during electrical heating [Fig. S1(d)] as well as uncapped Sb_2Te_3 (partially oxidized at the surface, Fig. S1(c)). These GST and Sb_2Te_3 films were also measured by XPS and show evidence of surface oxidation (Fig. S2).

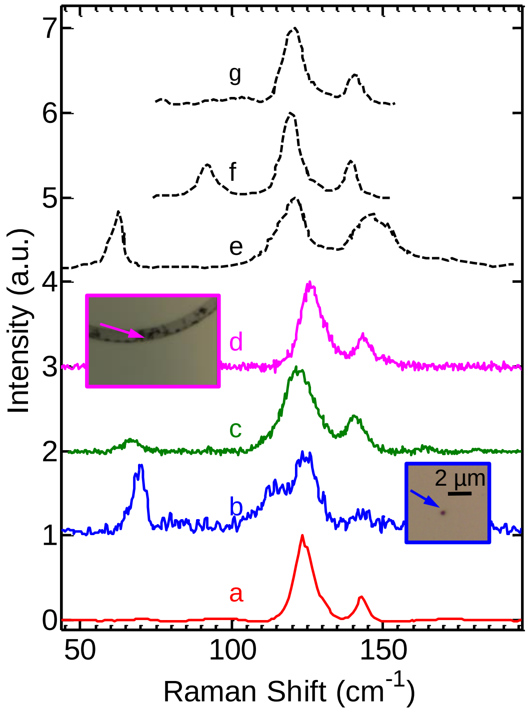

Figure S1 | Raman signatures of oxidized GST, Sb_2Te_3 and Te. Raman spectra of: (a) Patterned and finalized GST device described in the main text, after lift-off, (b) dark spot formed in uncapped GST film (inset, blue) following Raman measurement at high laser power (~10 mW). (c) Sb_2Te_3 uncapped film, (d) dark spot formed in uncapped GST circular device (inset, purple) after showing resistance changes induced by electrical pulses, (e) amorphous Te[8], (f) trigonal z-axis of Te[8], and (g) trigonal x-axis of Te[8].

Figure S2 shows X-Ray photoelectron spectroscopy (XPS) data of uncapped GST device (20 nm) thick) before and after a short Ar sputtering etch. The pre-sputter results represent the GST surface. Both Ge and Sb show native oxide peaks, whereas Te does not. Post-sputtering (i.e. a few nm into the film) the Sb_2O_3 + Sb_2O_5 peak decays and Ge + GeO_x feature narrows, suggesting the native oxide is only present at the top few nm of the film. We note that the sputtering can also induce some damage to the film, so these results are mostly qualitative. Overall, Fig. S1 and Fig. S2 suggest that surface oxidation of GST results in formation of native Ge and Sb oxides as well as Te precipitates. These Te precipitates dominate the Raman signal.

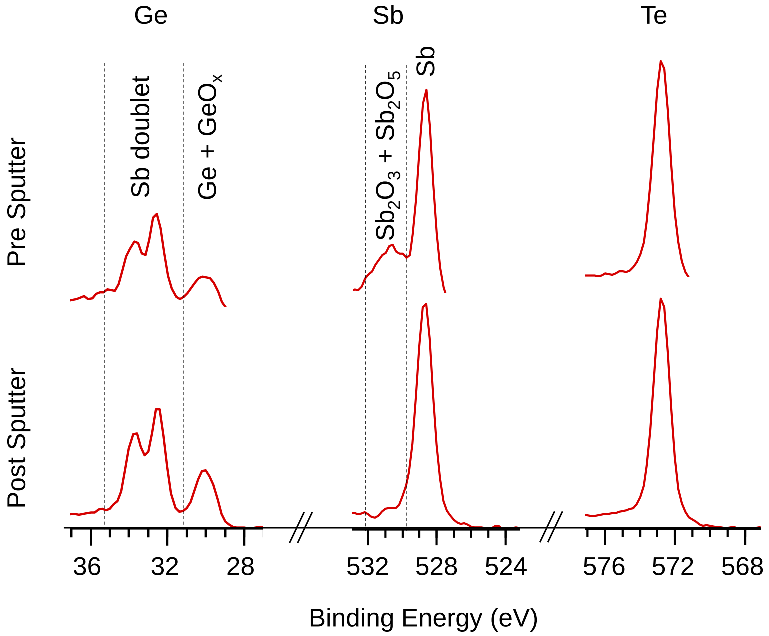

Figure S2 | XPS of uncapped (oxidized) GST. Pre-sputter (top panel) represents the GST surface, showing features of native Ge and Sb oxides as well as (un-oxidized) Te. The post-sputtering measurement (bottom panel) probes a few nm into the film, but might induce damage at the surface. The Sb_2O_5 + Sb_2O_3 feature decays and Ge + GeO_x feature narrows post-sputtering, suggesting Sb and Ge are oxidized only at the very top surface.

3. Frequency dependence of the anti-Stokes to Stokes intensity ratio

The temperature in our experiment is measured by comparing the Raman *peak shifts* in an electrically biased sample to a calibration measurement on a hot stage. The anti-Stokes to Stokes (AS/S) Raman intensity ratio can also be used to probe temperature, without the need for a calibration measurement (on a hot stage) and/or a reference measurement (without electrical bias). In our experiment the uncertainty in temperature measured by I_{AS}/I_S is significantly larger than the one measured by the peak shift method. One reason is that the uncertainty in measured (and fitted) intensity is larger compared with the measurement and fitting of (spectral) peak position. In addition, we illustrate in Fig. S3 that the temperature sensitivity in the AS/S method is poor for low wavenumbers (in our experiment the peaks are located at ~120 and 140 cm^{-1}). We note that for materials with Raman modes at higher frequency, the AS/S method could potentially be used with lower uncertainty. On the other hand, the AS signal intensity degrades with increasing mode frequency due to the decrease in phonon absorption probability.

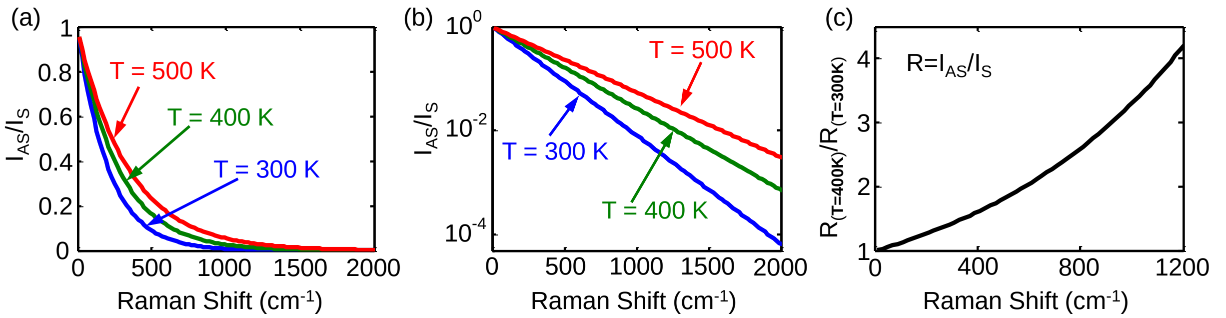

Figure S3 | Anti-Stokes to Stokes (I_{AS}/I_S) signal sensitivity. Calculated I_{AS}/I_S vs. Raman shift (peak position) at T = 300 K (blue), 400 K (green), and 500 K (red) in (a) linear and (b) log y-axis. The temperature sensitivity improves with increasing wavenumber, but the I_{AS} signal intensity decreases. (c) Sensitivity to temperature rise of ~ 100 K above room temperature; plot shows the ratio between $R = I_{AS}/I_S$ at 400 K and 300 K vs. Raman shift of the measured mode.

4. Scanning thermal microscopy (SThM)

Scanning thermal microscopy (SThM) is an atomic force microscopy (AFM) based technique that uses a thermo-resistive probe to acquire nanoscale topographic and thermal images simultaneously[9,10]. When the probe is brought into contact with the sample surface, heat is exchanged between the surface and the probe. These temperature changes are correlated with the electrical resistance of the probe, which is measured using a Wheatstone bridge. The SThM has two main operating modes: one active, in which the probe is heated up and acts as both the heater and the thermometer, and the other passive, in which the probe is only used as the temperature sensor. The probe or sample heating can be carried out by DC or AC currents, which allow multiple ways of measuring and processing data. The SThM technique has been used to measure the thermal properties of films[11,12], nanowires[13,14], and devices[15]. In this study, the PCM device is Joule-heated in DC mode and the probe is used passively for sensing the local temperature rise. The SThM signal calibration (mV to K) is done via the Raman temperature measurement and we assume this calibration is the same on both areas of the GST: on top of the contact and on top of the channel (all capped by ~ 150 nm PMMA).

5. SThM images

Figure S4 displays SThM maps at varying input power and the corresponding AFM topography map. The heating maps show significant heating at the contact edges.

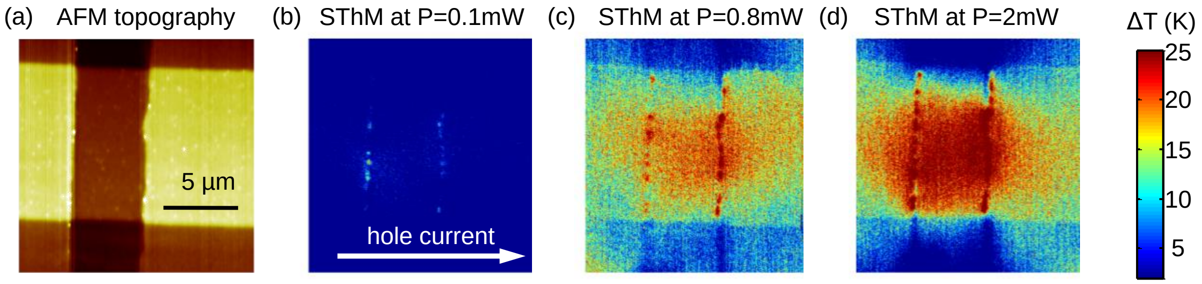

Figure S4 | AFM and SThM. (a) AFM topography map of the GST device described in the main text. Scanning thermal microscopy (SThM) maps of the same GST device with varying power inputs: (b) P = 0.1 mW, (c) P = 0.8 mW, and (d) P = 2 mW. The SThM heating map is calibrated via the Raman temperature measurement to obtain temperature values. Arrow in (b) indicates hole current flow direction for all 3 maps shown. The thermal maps show significant heating at the contact edges.

6. Temperature maps

We obtained temperature maps of the GST devices by Raman and SThM. Representative temperature profiles along the device (obtained by averaging temperature across device width) are shown in Fig. 4 of the manuscript. Figure S5 below compares measured and simulated temperature maps obtained by (b,c) SThM and (e,f) Raman. The (a) AFM topography map and (d) Raman intensity map are shown as reference to locate the channel and contact areas. Figure S6 displays a reference SThM scan when the device is unbiased (no Joule heating) showing only small artificial temperature rise (< 1 K) as a result of topography changes across the device. The step-height artifact is reduced here thanks to the surface planarization achieved by the PMMA capping layer.

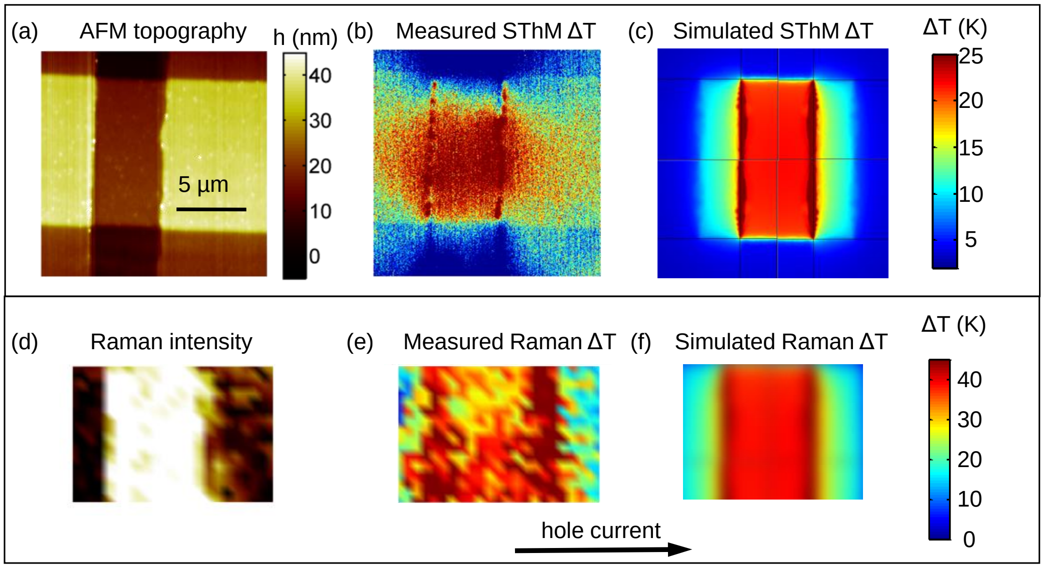

Figure S5 | Temperature maps: SThM, Raman and simulations. (a) AFM topography map of the GST device described in the main text. (b) Measured and (c) simulated SThM map of the same device at input power P = 2 mW. (d) Intensity map of the Raman mode at ~122 cm^{-1}. (e) Measured and (f) simulated Raman temperature map of the same device at input power P = 3.6 mW. Arrow indicates hole current flow.

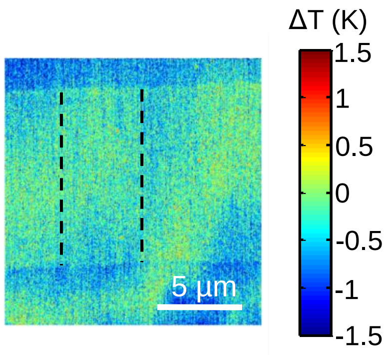

Figure S6 | Reference SThM map. Measured SThM map of the device when it is unbiased (no Joule heating) under the same probe sensing conditions of the maps shown in Fig. S5. The map shows small changes in the temperature < ~ 1 K as a result of topography changes or other artifacts. Black dashed lines indicate the edges of the electrodes.

7. Transfer length method (TLM)

Figure S7 displays TLM measurements of our GST films, showing the electrical resistance vs. channel length to obtain contact and sheet resistances. It is evident that in our lateral GST devices, for channels shorter than ~ 5 µm the contacts account for more than 50% of the total resistance, and therefore most of the power will be dissipated at the contacts. The extracted resistivity of the GST $\rho \approx 35$ mΩ·cm agrees with previous studies[16] given the annealing temperature (180 °C for 10 minutes, leading to fcc phase) used here. The *contact resistivity* could not be reliably evaluated from the measured *contact resistance* due to the poor coverage of the GST film on the Pt contact sidewall and the resulting current crowding at the contact edge.

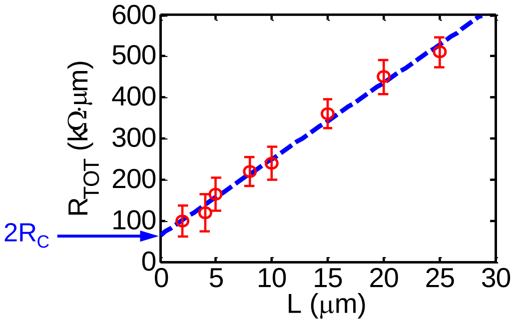

Figure S7 | Transfer length method (TLM). Electrical resistance (normalized by width) of our GST test structures with varying channel length to obtain contact and sheet resistivity. The y-axis intercept represents the resistance of the contacts ($2R_C$), and the sheet resistance can be obtained from the slope.

8. PCM device breakdown

The lateral PCM devices undergo breakdown at high electrical bias, rather than reset to amorphous state. These devices degrade when the GST channel is self-heated, ostensibly because the PMMA capping layer evaporates, leaving the GST exposed to air at high temperature, at which it oxidizes. Optical images of the devices post-breakdown reveal damage to the GST film near the ground terminal, as shown in Fig. S8(a). The location of the breakdown spot agrees well with the measured peak temperature [Fig. S8(b)].

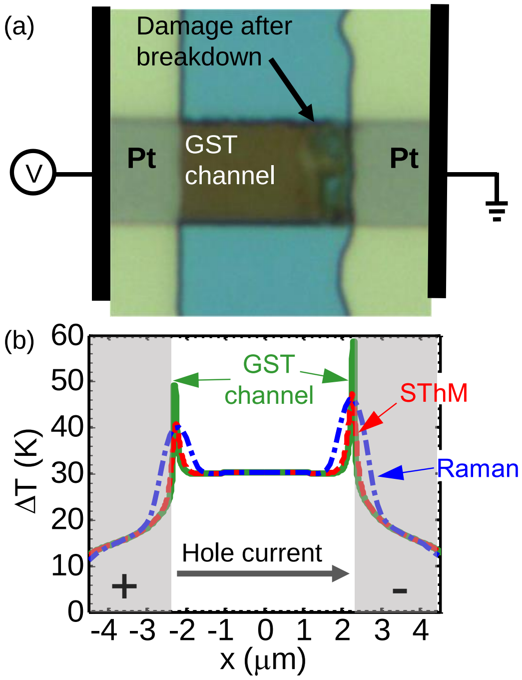

Figure S8 | Post-breakdown damage. (a) Optical image of GST channel after breakdown showing damage near the grounded electrode. (b) Simulated temperature profile (calibrated by measurements) of the GST channel (see Fig. 5 in the main text for details) showing the peak temperature located near the grounded terminal.

9. Parameters used in COMSOL simulation

Table I – parameters used in finite element modeling simulations (near room temperature)

Parameter	Description	Value	Reference\comments
ρ_{GST}	GST Electrical specific resistivity	35 mΩ·cm	TLM measurement (fcc)
$\rho_{C,GST}$	Electrical contact resistivity between GST-Pt	$4\cdot10^{-4}$ Ω·cm^2	TLM measurement (fcc)
ρ_{Pt}	Pt Electrical specific resistivity	$1.8\cdot10^{-7}$ Ω·cm	4-probe measurement of similar films
k_{GST}	GST thermal conductivity	1 Wm^{-1}K^{-1}	We set k_{GST} = 1 Wm^{-1}K^{-1}, (Ref. 17) but the simulated temperature rise in the lateral device is relatively insensitive (less than 10% change) to thermal conductivity changes in the range k_{GST} ~ 0.5 to 1.5 Wm^{-1}K^{-1}
k_{Pt}	Pt thermal conductivity	50 Wm^{-1}K^{-1}	Estimated from measured ρ_{Pt} via

			Wiedemann Franz law
k_{PMMA}	PMMA thermal conductivity	0.19 Wm^{-1}K^{-1}	COMSOL materials library Steady state temperature profile is insensitive to this parameter
k_{SiO2}	SiO$_2$ thermal conductivity	1.4 Wm^{-1}K^{-1}	Ref. 18
k_{Si}	Si (p^{++}) thermal conductivity	95 Wm^{-1}K^{-1}	Ref. 5
TBR GST-SiO$_2$	Thermal boundary resistance (TBR) of GST-SiO$_2$ interface	28 m^{2}K/GW	Determined by fitting the temperature at the center of the channel to experimental data. Error ±8 m^{2}K/GW
TBR GST-Pt	TBR of GST-Pt interface	25 m^{2}K/GW	Determined by fitting the temperature profile at the contact area to experimental data. Error ±9 m^{2}K/GW
TBR Si-SiO$_2$	TBR of Si-SiO$_2$ interface	3 m^{2}K/GW	Ref. 18
TBR GST-PMMA	TBR of GST-PMMA interface	25 m^{2}K/GW	Set to similar value as GST-Pt, but steady state temperature profile is insensitive to this parameter

Supplementary References

1 Schadler, L. & Galiotis, C. Fundamentals and applications of micro Raman spectroscopy to strain measurements in fibre reinforced composites. *International Materials Reviews* **40**, 116-134 (1995).

2 Basko, D., Piscanec, S. & Ferrari, A. Electron-electron interactions and doping dependence of the two-phonon Raman intensity in graphene. *Physical Review B* **80**, 165413 (2009).

3 Dresselhaus, M., Jorio, A., Cançado, L., Dresselhaus, G. & Saito, R. in *Graphene Nanoelectronics* 15-55 (Springer, 2011).

4 Freitag, M., Steiner, M., Martin, Y., Perebeinos, V., Chen, Z., Tsang, J. C. & Avouris, P. Energy dissipation in graphene field-effect transistors. *Nano Letters* **9**, 1883-1888 (2009).

5 Yalon, E., McClellan, C. J., Smithe, K. K., Munoz-Rojo, M., Xu, R., Suryavanshi, S. V., Gabourie, A. J., Neumann, C. M., Xiong, F., Farimani, A. B. & Pop, E. Energy Dissipation in Monolayer MoS$_2$ Electronics. *Nano Letters* **17**, 3429–3433 (2017).

6 Kip, B. J. & Meier, R. J. Determination of the local temperature at a sample during Raman experiments using Stokes and anti-Stokes Raman bands. *Applied Spectroscopy* **44**, 707-711 (1990).

7 Tsai, C.-L., Liao, A., Pop, E. & Shim, M. Electrical power dissipation in semiconducting carbon nanotubes on single crystal quartz and amorphous SiO2. *Applied Physics Letters* **99**, 053120 (2011).

8 Pine, A. & Dresselhaus, G. Raman spectra and lattice dynamics of tellurium. *Physical Review B* **4**, 356 (1971).

9 Majumdar, A. Scanning thermal microscopy. *Annual Review of Materials Science* **29**, 505-585 (1999).

10 Borca-Tasciuc, T. Scanning probe methods for thermal and thermoelectric property measurements. *Annu. Rev. Heat Transfer* **16**, 211-258 (2013).

11 Wilson, A. A., Rojo, M. M., Abad, B., Perez, J. A., Maiz, J., Schomacker, J., Martín-Gonzalez, M., Borca-Tasciuc, D.-A. & Borca-Tasciuc, T. Thermal conductivity measurements of high and low thermal conductivity films using a scanning hot probe method in the 3 ω mode and novel calibration strategies. *Nanoscale* **7**, 15404-15412 (2015).

12 Volz, S., Feng, X., Fuentes, C., Guérin, P. & Jaouen, M. Thermal conductivity measurements of thin amorphous silicon films by scanning thermal microscopy. *International Journal of Thermophysics* **23**, 1645-1657 (2002).

13 Muñoz Rojo, M., Grauby, S., Rampnoux, J.-M., Caballero-Calero, O., Martin-Gonzalez, M. & Dilhaire, S. Fabrication of Bi2Te3 nanowire arrays and thermal conductivity measurement by 3ω-scanning thermal microscopy. *Journal of Applied Physics* **113**, 054308 (2013).

14 Rojo, M. M., Martín, J., Grauby, S., Borca-Tasciuc, T., Dilhaire, S. & Martin-Gonzalez, M. Decrease in thermal conductivity in polymeric P3HT nanowires by size-reduction induced by crystal orientation: new approaches towards thermal transport engineering of organic materials. *Nanoscale* **6**, 7858-7865 (2014).

15 Menges, F., Mensch, P., Schmid, H., Riel, H., Stemmer, A. & Gotsmann, B. Temperature mapping of operating nanoscale devices by scanning probe thermometry. *Nature Communications* **7**, 10874 (2016).

16 Roy, D., in't Zandt, M., Wolters, R., Timmering, C. & Klootwijk, J. in *2009 Non-Volatile Memory Technology Symposium (NVMTS).* 12-15 (IEEE, DOI:10.1109/NVMT.2009.5429780).

17 Reifenberg, J. P., Panzer, M. A., Kim, S., Gibby, A. M., Zhang, Y., Wong, S., Wong, H.-S. P., Pop, E. & Goodson, K. E. Thickness and stoichiometry dependence of the thermal conductivity of GeSbTe films. *Applied Physics Letters* **91**, 111904 (2007).

18 Chien, H.-C., Yao, D.-J., Huang, M.-J. & Chang, T.-Y. Thermal conductivity measurement and interface thermal resistance estimation using SiO_2 thin film. *Review of Scientific Instruments* **79**, 054902 (2008).